

Band Renormalization in Metal–Organic Framework/Au(111) Epitaxial Heterostructures

Xiaoqing Yuan^{1,2,3,†}, Shaoze Wang^{2,3,4,†,*}, Xiaoyue He⁵, Zhecheng Sun^{3,4}, Lei Sun^{2,3,4,*}

¹Department of Physics, Fudan University, Shanghai 200433, China

²Department of Physics, School of Science and Research Center for Industries of the Future, Westlake University, Hangzhou 310030, Zhejiang Province, China

³Institute of Natural Sciences, Westlake Institute for Advanced Study, Hangzhou 310024, Zhejiang Province, China

⁴Department of Chemistry, School of Science and Research Center for Industries of the Future, Westlake University, Hangzhou 310030, Zhejiang Province, China

⁵Songshan Lake Materials Laboratory, Dongguan 523808, Guangdong Province, China

[†]These authors contributed equally to this work.

*Email: sunlei@westlake.edu.cn; wangshaoze@westlake.edu.cn

Abstract

Two-dimensional conjugated metal–organic frameworks hold great promise for applications in chemiresistive sensing, electrocatalysis, and energy storage. Their interfacial interaction with metal electrodes, which has been rarely investigated, exerts a critical influence on the electronic properties and device performance. As a representative material, $M_3(\text{HITP})_2$ ($M = \text{Ni}, \text{Cu}$; HITP = 2,3,6,7,10,11-hexaiminotriphenylene) exhibits excellent performance in various electronic devices, yet the microscopic mechanism of the interfacial interaction in $M_3(\text{HITP})_2/\text{metal}$ heterostructures remains unclear. Here, we report the synthesis, scanning tunneling microscopic characterization, and tight-binding analysis of monolayer $M_3(\text{HITP})_2$ epitaxially grown on Au(111). Scanning tunneling spectroscopic mapping reveals a commensurate kagome-hexagonal-honeycomb triple-lattice architecture. The Au(111) substrate renormalizes the electronic band structure of $M_3(\text{HITP})_2$, pinning the Fermi level and generating a ligand-derived flat band at 0.4 eV that corrects prior misassignment of orbital character. Meanwhile, the periodic and microporous $M_3(\text{HITP})_2$ lattice strongly modulates the surface electronic state of Au(111) via electron-phonon coupling and quantum confinement, the latter of which gives rise to a quantum corral network exhibiting two resonant states within each pore. The formation of fully dispersive electronic bands and the robust quantum corral network requires crystallites comprising at least ten pores. The atomic-scale investigation of $M_3(\text{HITP})_2/\text{Au}(111)$ epitaxial heterostructures elucidates interlayer coupling mechanisms and advances the understanding of metal–organic framework/metal interfaces that are integral to electronic and energy-storage devices.

Introduction

Two-dimensional (2D) conjugated metal–organic frameworks (MOFs)—crystalline layered materials formed via the coordination-driven self-assembly of metal ions and conjugated organic ligands—exhibit highly ordered and crystallographically diverse lattices (e.g. kagome, hexagonal, honeycomb, and Lieb lattices) with in-plane metal–ligand covalency¹. Compared with conventional inorganic 2D materials, the lattice geometry and electronic band structures of 2D MOFs can be rationally designed at the atomic level, leading to the observation of a broad range of electronic behaviors resembling semiconductors, metals, and even superconductors^{2–8}. These electronic functionalities have extended the applications of MOFs beyond traditional areas such as gas storage and separation, towards electronic and energy devices spanning field-effect transistors, chemiresistive sensors, supercapacitors, and electrocatalysis^{9–16}. Many of these applications involve interfaces between MOFs and electrode materials, resulting in the formation of MOF/metal heterostructures. Such heterostructures can profoundly modify the electron behaviors of the constituent materials through interfacial charge transfer, lattice symmetry reconstruction, and periodic modulation of charge density, which reconfigures Coulombic and magnetic interactions at distinct atomic sites^{17–21}. This reconfiguration can significantly renormalize the electronic band structure, potentially altering charge transport and magnetic behaviors of the MOF and ultimately influencing its performance in electronic devices. Nevertheless, these interfacial phenomena remain largely unexplored. Macroscopic transport measurements typically capture only the ensemble-averaged electron behaviors, offering limited insight into microscopic mechanisms. To this end, the nanoscale construction of MOF/metal heterostructures provides an ideal quantum platform for probing interfacial interactions and microscopic investigations of electronic band structures²².

$M_3(\text{HITP})_2$ ($M = \text{Co}, \text{Ni}, \text{Cu}$; HITP = 2,3,6,7,10,11-hexaiminotriphenylene) stands as a promising material platform for investigating MOF/metal heterostructures, owing to its well-defined lattice symmetry, excellent electrical properties, and emerging relevance as a quantum material^{9,23–25}. The framework is formed through the coordination of square-planar metal ions with tridentate conjugated ligands, yielding a layered structure that coherently integrates three distinct lattices—a metal-centered kagome lattice, a ligand-derived honeycomb lattice, and a

hexagonal lattice of vacant pores (Fig. 1)—a structural motif difficult to accomplish in conventional 2D materials. This unique architecture has been predicted to host exotic quantum phenomena including nontrivial band topology and quantum anomalous Hall effect^{24,26–29}. In addition, $M_3(\text{HITP})_2$ exhibits relatively high room-temperature electrical conductivity, which has been attributed to intralayer π -d conjugation and interlayer π - π stacking^{25,30,31}. The combination of electrical conductivity and inherent microporosity has enabled high performance of $M_3(\text{HITP})_2$ in a variety of applications including supercapacitors, electrocatalysis, and chemiresistive sensing among others^{9,15,32}.

Previous studies have demonstrated the ultrahigh-vacuum synthesis of $M_3(\text{HITP})_2$ on Au(111), enabling structural analysis and spectroscopic characterization of the as-grown crystallites^{33–35}. These experimental efforts, corroborated by density functional theory (DFT) calculations, have led to the proposal of a metal-centered kagome flat band located at approximately 0.6 eV above the Fermi level^{24,35–37}. However, the lack of high-resolution local density-of-states (LDOS) mapping and comprehensive band structure analysis has hindered unambiguous assignment of orbital characters and band topology. From a theoretical perspective, the distinct work functions of the MOF and the metal substrate are expected to induce interfacial charge transfer, potentially shifting the Fermi level of the MOF. Meanwhile, mutual modulation of charge density distributions in the MOF and metal substrate should reconstruct their band structures and in return alter electron behaviors^{20,22}. A deeper understanding of these effects demands a systematic investigation into band renormalization in $M_3(\text{HITP})_2$ /metal heterostructures.

Herein, we report the nanoscale construction and scanning tunneling microscopic (STM) characterization of $M_3(\text{HITP})_2$ /Au(111) ($M = \text{Ni}$ or Cu) epitaxial heterostructures, revealing an energy-tunable kagome-hexagonal-honeycomb triple-lattice architecture, renormalized band structures, and size-dependent electron behaviors. Molecular beam epitaxy (MBE) synthesis of $M_3(\text{HITP})_2$ on Au(111) surface in ultrahigh vacuum led to monolayer crystallites whose Fermi levels are significantly shifted and pinned by the substrate. Scanning tunneling spectroscopic (STS) mapping and quasiparticle interference (QPI) analysis articulated orbital characters of bands near the Fermi level. Corroborated by tight-binding analysis, they revealed the

modulation of surface states of Au(111) by the MOF lattice, interlayer electron-phonon coupling, as well as the formation of quantum corral networks manifested as in-pore resonant states. Tracking gradual evolution of LDOS from small crystallites to extended frameworks showed that fully dispersive electronic bands and quantum corral networks emerge in $M_3(\text{HITP})_2/\text{Au}(111)$ heterostructures comprising ten regular porous nanostructures. These observations provide direct evidence of mutual modulation of band structures between $M_3(\text{HITP})_2$ and Au(111), establishing a framework for understanding MOF/metal interface in electronic devices.

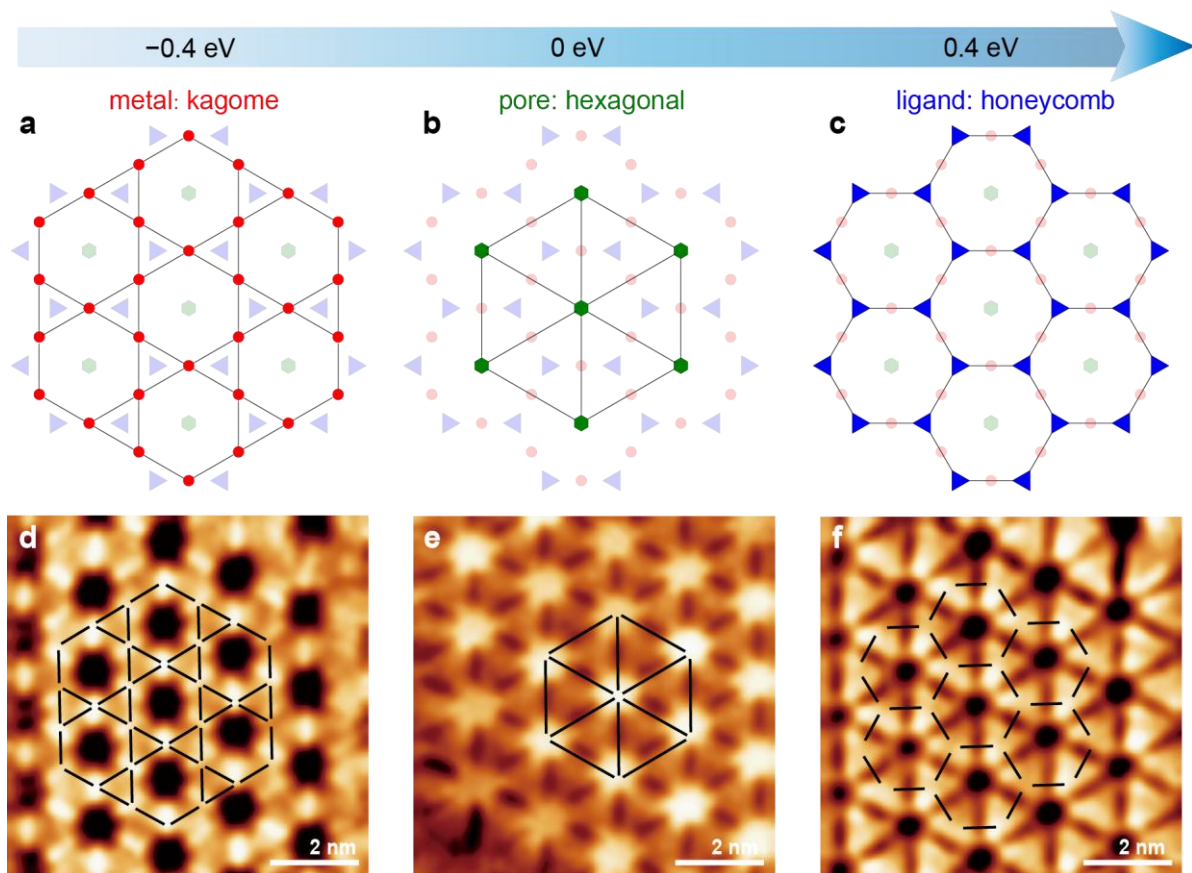


Fig. 1 | Energy-tunable triple lattices realized in $M_3(\text{HITP})_2/\text{Au}(111)$ heterostructure. **a**, Schematic of kagome lattice formed by metal ions, **b**, hexagonal lattice formed by resonant states in pores, **c**, honeycomb lattice formed by HITP ligands. **d–f**, Highlighted kagome, hexagonal, and honeycomb lattices overlaid on images acquired in STS mappings with $V_s = -0.4$ V, $I_t = 100$ pA (I channel), $V_s = 0$ V, $I_t = 100$ pA (dI/dV channel), and $V_s = 0.4$ V, $I_t = 100$ pA (dI/dV channel), respectively. V_s : voltage of sample; I_t : current of tip.

Synthesis and structural characterization

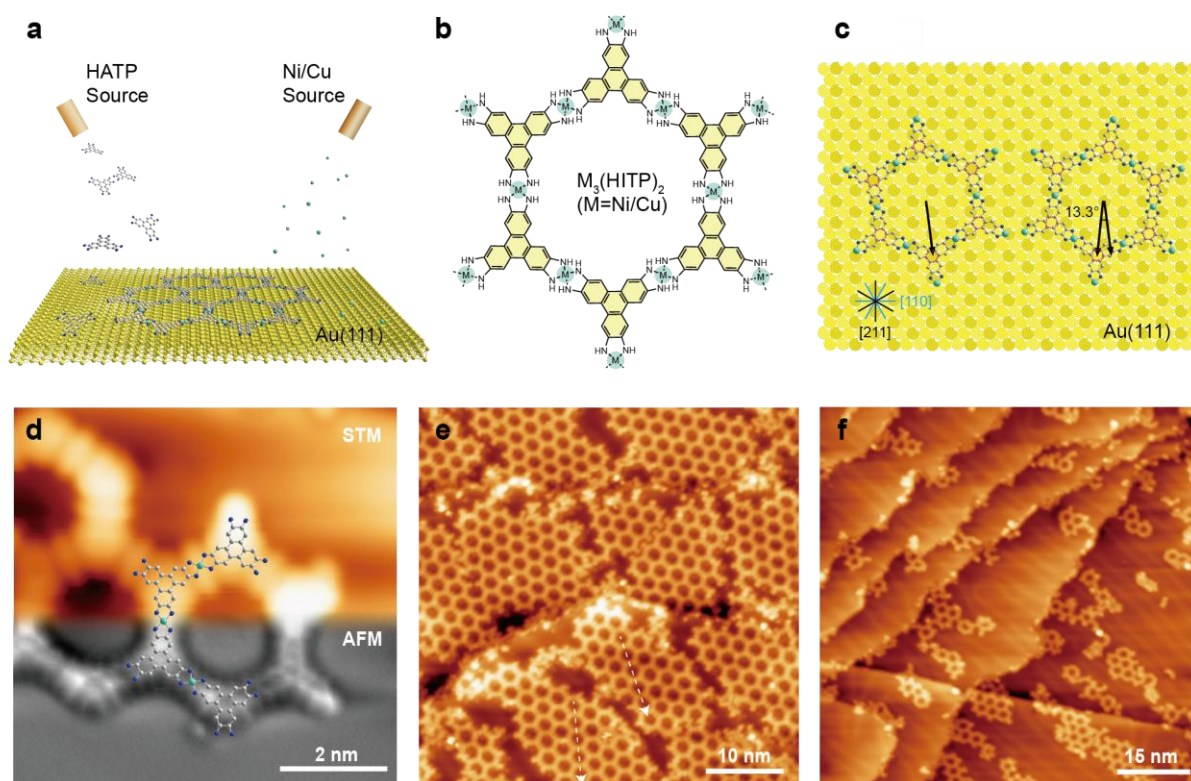


Fig. 2 | Synthesis and structural characterization of monolayer $M_3(\text{HITP})_2$ on Au(111). **a**, Schematic of the MBE growth of $M_3(\text{HITP})_2$. **b**, Structure of monolayer $M_3(\text{HITP})_2$, featuring a honeycomb lattice formed by HITP ligands (yellow) and a kagome lattice formed by metal ions (blue). **c**, Two adsorption orientations of $M_3(\text{HITP})_2$ on Au(111), rotated by 13.3° relative to each other. Light blue, gray, dark blue, and yellow spheres represent Ni/Cu, C, N, and Au, respectively. H atoms are omitted for clarity. **d**, The STM (top) and q-Plus AFM (bottom) images of $\text{Ni}_3(\text{HITP})_2$ acquired in the same region, with corresponding atomic model overlaid. **e**, High coverage of $\text{Ni}_3(\text{HITP})_2$ domains on Au(111) with two different orientations marked by white arrows. **f**, Low coverage of $\text{Ni}_3(\text{HITP})_2$ domains on Au(111) with crystallites consisting of a small number of pores. All the STM images were acquired with $V_s = -1$ V, $I_t = 100$ pA.

We synthesized $M_3(\text{HITP})_2$ by depositing metal atoms ($M = \text{Ni}$ or Cu) and 2,3,6,7,10,11-hexaaminotriphenylene (HATP) molecules onto atomically clean Au(111) substrate in ultra-high vacuum (UHV) followed by annealing at 240 °C where Ni or Cu deprotonates, reduces, and binds HATP (Fig. 2a; see Methods and Supplementary Information). Q-plus atomic force microscopy (AFM) verified structural integrity of ligands and revealed square-planar $[\text{MN}_4]$ building blocks formed by two HITP (deprotonated HATP) ligands coordinating to each metal ion (Fig. 2d). STM topographic imaging in the same region confirmed this structure (Fig. 2d). The HITP ligand exhibits an equilaterally triangular electron cloud that is rotated by 60° with respect to its atomic structure³³. Electron cloud of the metal ion is squeezed into an oblate spherical orbital^{33,38}. The self-assembly of these two constituents generates an ordered network. Both $\text{Ni}_3(\text{HITP})_2$ and $\text{Cu}_3(\text{HITP})_2$ share the same topography featuring two interlocked lattices: a kagome lattice formed by the metal nodes and a honeycomb lattice formed by the organic ligands (Fig. 2b; Fig. 1d and 1f). They delineate hexagonal pores that form a hexagonal lattice whose unit cell parameter (namely distance between center of adjacent pores) is 2.2 nm. The extension of electron cloud from the pore edges shrinks the pore diameter to approximately 1.5 nm (Supplementary Fig. 2c).

In regions on the hexagonal Au(111) surface with a high coverage of $M_3(\text{HITP})_2$, crystalline domains adopt two orientations where their symmetry axes rotate by 13.3° with respect to each other (Fig. 2e). The lateral size of each domain is primarily 10 – 20 nm. This phenomenon can be rationalized by an adsorption model where the central benzene ring of each HITP ligand is positioned precisely atop a gold atom (Fig. 2c), i.e. the energetically favorable atomic site for the extended π -conjugated system under van der Waals interactions with the substrate³³. This model indicates the formation of $M_3(\text{HITP})_2/\text{Au}(111)$ commensurate heterostructures and yields two lowest-energy adsorption configurations that are oriented at angle of 13.3° relative to each other, consistent with the experimental observation. Such flexible crystallographic orientations prohibit the growth of large-area single crystals at the atomic level. In addition, decreasing the precursor dosage generated a lower coverage of $M_3(\text{HITP})_2$ whose crystallites mainly contain 1 to 10 hexagonal pores (Fig. 2f). This facilitates subsequent studies on the relationship between electronic band structure and crystallite size.

Quasiparticle interference at $\text{Cu}_3(\text{HITP})_2/\text{Au}(111)$ heterostructure

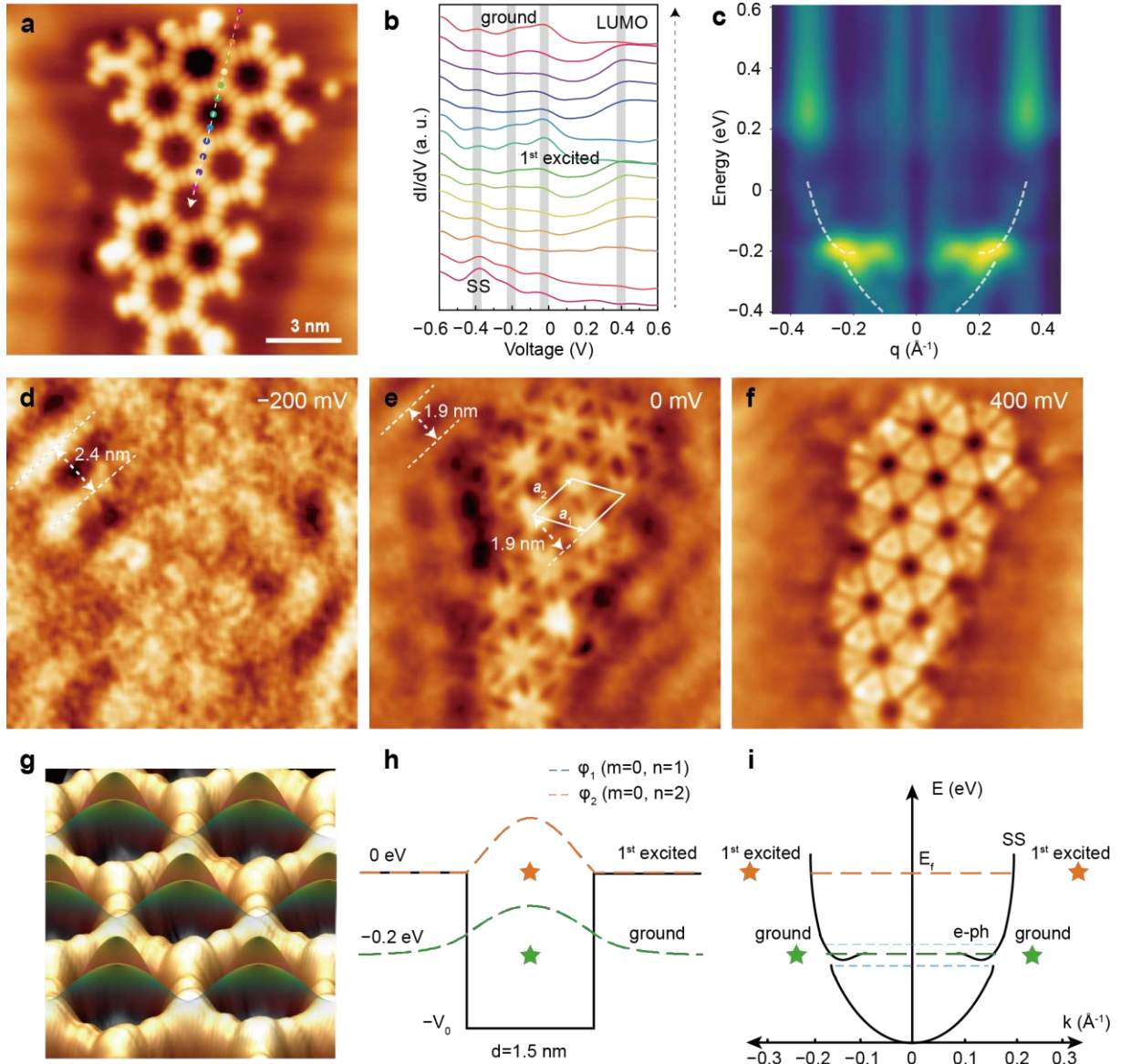


Fig. 3 | Energy-dependent LDOS measurements and QPI analysis of $\text{Cu}_3(\text{HITP})_2$. **a**, STM topography of a 10-pore $\text{Cu}_3(\text{HITP})_2$ crystallite. **b**, Spatially resolved dI/dV spectra acquired along the color-coded path marked in **a**. Gray shaded regions indicate four characteristic energy positions. SS and LUMO represent surface state and the lowest unoccupied molecular orbital, respectively. LDOS features corresponding to the ground and the first excited resonant states are indicated. **c**, QPI pattern obtained by FFT of energy-dependent STS mappings, overlaid with the parabolic band dispersion (white dashed line) of the Au(111) surface state. **d–f**, Real-space STS mappings of the region in **a** acquired at -200 mV, 0 mV, and 400 mV, respectively. All the STM images and STS measurements were acquired with $V_s = -1$ V, $I_t = 100$ pA. **g**,

Three-dimensional scheme of resonant states inside MOF pores. **h**, 2D quantum corral configuration with two quantized standing waves. **i**, E - k plot of Au(111) surface state, quantized resonant states, and quasiparticles with electron-phonon coupling-induced distorted momenta. Green and orange stars represent the ground and the first excited resonant states, respectively. Blue dash lines point to the quasiparticles with relative flat band apart from the normal parabolic dispersion.

We then focused on a $\text{Cu}_3(\text{HITP})_2$ crystallite containing 10 pores and analyzed its energy-dependent electronic LDOS by differential conductance (dI/dV) line scanning and 2D mapping. 14 spatially consecutive dI/dV spectra were acquired along a path crossing from the bare Au(111) substrate to the MOF crystallite, encompassing HITP ligands, Cu nodes, and center of pores (Fig. 3a,b; Supplementary Fig. 2). The clear signature of the Au(111) surface state observed atop the substrate is confirmed by the prominent peak at approximately -0.4 eV. This surface state has a diffusive influence on the entire MOF crystallite and manifests itself as a DOS peak at the same energy in all spectra. The DOS peak at 0.4 eV consistently appears over the MOF lattice yet vanishes inside pores. In contrast, the broad DOS peaks at approximately -0.2 eV and 0 eV are salient inside pores while almost absent over the MOF lattice.

To further explore the origin of LDOS features, we performed STS mapping from -0.4 eV to 0.6 eV. The LDOS at -0.2 eV does not show a clear contrast over the region, indicating comparable contributions of electronic states of metal ions, HITP ligands, and the Au(111) substrate in pores (Fig. 3d). STS mapping at the Fermi level reveals regions with pronounced LDOS intensity confined within pores, which are connected to each other through HITP ligands with much weaker LDOS (Fig. 3e). Signatures of electron standing waves with wavelengths of 2.4 nm and 1.9 nm were observed at -0.2 eV and the Fermi level, respectively, on Au(111) near the $\text{Cu}_3(\text{HITP})_2$ crystallite (Fig. 3d,e), indicating modulation of the gold surface state by the MOF lattice. At 0.4 eV, intense LDOS regions resemble equilateral-triangle features on HITP ligands (Fig. 3f) that are consistent with the observation from STM topographic imaging (Fig. 2d). The LDOS at metal nodes is negligible from 0 eV to 0.6 eV. These observations confirm the assignment of DOS peaks at 0.4 eV and 0 eV to the localized lowest unoccupied molecular orbital (LUMO) of HITP ligands (*vide infra*) and electronic states derived from the gold substrate, respectively. Notably, the former assignment is distinct from previous attribution of

a metal-based kagome flat band at 0.6 eV, reinforcing the indispensability of high-resolution STS mapping for understanding electronic band structures of 2D MOF on metal surface. Similar phenomena were observed in $\text{Ni}_3(\text{HITP})_2/\text{Au}(111)$ heterostructures (Fig. 4d–f).

Fast Fourier transform (FFT) of STS mapping results gives rise to a QPI pattern across -0.4 eV to 0.6 eV (Fig. 3c). Along K – K' direction, two energy-independent features are present at $q \approx \pm 0.35 \text{ \AA}^{-1}$ and $E = 0.2 \text{ eV} - 0.6 \text{ eV}$ (q represents the periodicity of interference in momentum space), which are attributed to (100) crystal planes with an inter-plane spacing of 1.9 nm. The pattern below the Fermi level exhibits a parabolic dispersion centered at $q = 0 \text{ \AA}^{-1}$ whose energy spanning -0.4 eV to 0 eV. It is assigned to the Shockley surface state hosted by the Au(111) substrate, which is theoretically a parabolic energy–momentum (E – k) dispersion formed by 2D near-free electron gas confined to the surface layer (Fig. 3i)^{39,40}. The appearance of this QPI dispersion stems from the scattering of surface electrons by the MOF lattice. It reaches $q \approx \pm 0.33 \text{ \AA}^{-1}$ at the Fermi level, corresponding to an electron wavelength of 1.9 nm that coincides with the (100) spacing of $\text{Cu}_3(\text{HITP})_2$ (Fig. 3e). Such match between the electron wave on Au(111) surface and the MOF lattice leads to enhanced DOS inside pores at the Fermi level (Supplementary Fig. 3, 4).

The parabolic dispersion crosses with a relatively flat and intense feature near $E = -0.2$ eV and $q = \pm 0.27 \sim \pm 0.19 \text{ \AA}^{-1}$ along K – K' direction (Fig. 3c; Supplementary Fig. 3), which corresponds to distorted electron waves on Au(111) surface (Fig. 3d). Deviation from the E – q parabolic dispersion relation indicates electron-phonon coupling with a phonon excitation energy of -0.2 eV (Fig. 3c and 3i; see Supplementary Information for more details). This phonon (approximately 1600 cm^{-1}) lies in the mid-infrared region and is assigned to C=C and C=N stretching modes of $\text{Cu}_3(\text{HITP})_2$ ^{41,42}. Hence, local vibrational modes in the MOF effectively modulate the band structure of gold (Fig. 3d).

In addition, taking the confinement effect into account and considering the energy of Au(111) surface state (approximately -0.4 eV), the edges of each pore serve as a quantum corral with diameter of 1.5 nm and depth of 0.4 eV⁴³. The quantum confinement of Au(111) surface electrons within the pore generates resonant states whose ground state and 1st excited state emerge at -0.2 eV and 0 eV, respectively, which match experimentally observed DOS peaks (Fig. 3h; see details in Supplementary Information). These localized and quantized resonant

states appear as standing waves within each pore, causing charge accumulation inside pores⁴⁴ and contributing to distinct electron hopping modes (Fig. 3g). These resonant states inherit the geometry of $M_3(\text{HITP})_2$, forming a quantum corral network with hexagonal lattice^{45,46}. Notably, the 1st excited state coincides with the Fermi level, which is a comprehensive result of the pore size and electron distributions of $M_3(\text{HITP})_2$ as well as the surface energy of Au(111). It significantly improves the LDOS at the Fermi level, which, upon adsorption of guest molecules within pores, would potentially lead to strong electrostatic and redox interactions with guests, enhancing device performance such as chemiresistive sensitivity and electrocatalytic activity.

Tight-binding band structure analysis

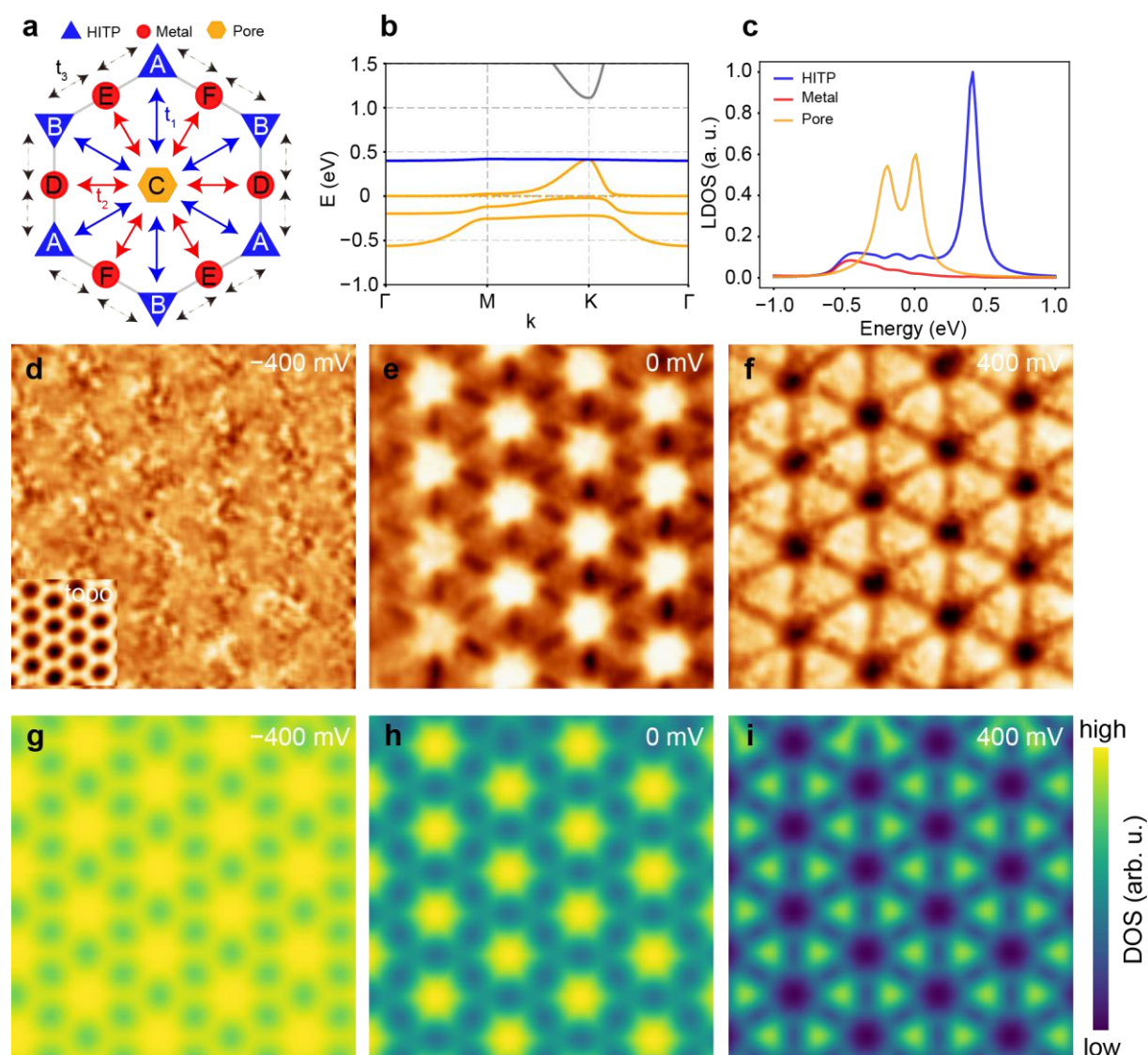


Fig. 4 | Band structure calculation of $M_3(\text{HITP})_2$ by tight binding model and comparison with LDOS mappings. **a**, Proposed kagome-hexagonal-honeycomb triple-lattice system of $M_3(\text{HITP})_2$. Blue triangles, red circles, and yellow hexagons represent HITP ligands, metal ions, and quasiparticles in the pores, respectively. t_1 , t_2 , and t_3 represent hopping constants between different sites. **b**, Band structure of $M_3(\text{HITP})_2$ along Γ —M—K— Γ high-symmetry points between -1.0 eV and 1.5 eV. **c**, LDOS of HITP ligands, metal atoms, and pores at different energies. **d–f**, Experimental STS mappings of $\text{Ni}_3(\text{HITP})_2$ at -400 mV, 0 mV, and 400 mV with corresponding topographic image shown as an inset in **d**. STS measurements were taken with $V_s = -1$ V, $I_t = 100$ pA. **g–i**, Theoretical calculations of LDOS mappings at -400 mV, 0 mV, and 400 mV.

We conducted tight-binding analysis to explore the electronic band structure near the Fermi level (-1 eV $-$ 1 eV) of the $M_3(\text{HITP})_2/\text{Au}(111)$ heterostructure. The STS mapping revealed negligible DOS from Ni or Cu as well as weak metal–ligand π – d conjugation between -0.2 eV and 0.6 eV. Hence, we propose that the MOF-modulated surface states of Au(111) play a key role in the band structure—they mediate electron hopping between different sites in the MOF, yielding stronger hopping than that within the framework, and couple with two pore-trapped resonant states. The overall kagome, hexagonal, honeycomb triple lattices of the heterostructure constitute an interlocked 8-band system with the following Hamiltonian (Fig. 4a):

$$H_{NN} = -V(C_1^\dagger C_{Au} + C_2^\dagger C_{Au}) - t_1(A^\dagger C_{Au} + B^\dagger C_{Au}) - t_2(D^\dagger C_{Au} + E^\dagger C_{Au} + F^\dagger C_{Au}) - t_3(D^\dagger A + E^\dagger A + F^\dagger A) - t_3(D^\dagger B + E^\dagger B + F^\dagger B) + h. c. \quad (1)$$

This electron system comprises of a gold surface state with parabolic dispersion (C_{Au}^\dagger), two resonant states (C_1^\dagger and C_2^\dagger), two HITP sites (A^\dagger and B^\dagger), and three Ni or Cu sites (D^\dagger , E^\dagger , and F^\dagger). Energies of the gold and ligand sites were respectively assigned to be k-dependent parabolic above -0.45 eV and 0.4 eV based on the STS mapping results, whereas those of Ni or Cu sites were arbitrarily assigned to be -1.6 eV such that they do not contribute to bands near the Fermi level to match the experimental observations. Hopping constants t_1 , t_2 and t_3 were assumed to be much larger than V , the latter of which describes the onsite coupling between surface states of Au(111) and resonant states inside pores. Only the nearest neighbor hopping was considered.

Near the Fermi level, this Hamiltonian yields a flat band at 0.4 eV and three dispersive bands between -0.6 eV and 0.4 eV within the first Brillouin zone (Fig. 4b). LDOS of the flat band almost exclusively stems from localized states of HITP (Fig. 4c). Phase cancellations of asymmetric wave functions from two different HITP sites in the honeycomb lattice inhibit electron hopping towards the hexagonal lattice, whereas perturbations from weak coupling with adjacent Ni or Cu sites induce a tiny dispersion. In contrast, LDOS of all dispersive bands are dominated by electronic states of Au(111) with slight contributions from both components of the MOF. The coupling between the surface state and resonant states generates energy gaps between adjacent bands. The band dispersion is inherited from the surface state, which endorses the $M_3(\text{HITP})_2/\text{Au}(111)$ heterostructure with metallicity.

The above model yields STS mapping simulations (Fig. 4g–i) that match experimental observations of $M_3(\text{HITP})_2/\text{Au}(111)$ heterostructure (Fig. 4d–f). Specifically, simulated images reproduce triangular HITP states at 0.4 eV and hexagram Au(111) states at the Fermi level. As gold, HITP, and metal ions contribute comparable LDOS at -0.4 eV, the simulated image at this energy shows a low contrast, which explains the featureless experimental image. Such consistency between simulated and experimental STS mapping confirms the validity of our model. It implies that the electrical conduction of $M_3(\text{HITP})_2/\text{Au}(111)$ heterostructures is predominantly governed by electrons from Au(111) and HITP—insufficient orbital overlap between metal ions and ligands near the Fermi level prevents efficient electron hopping within the framework.

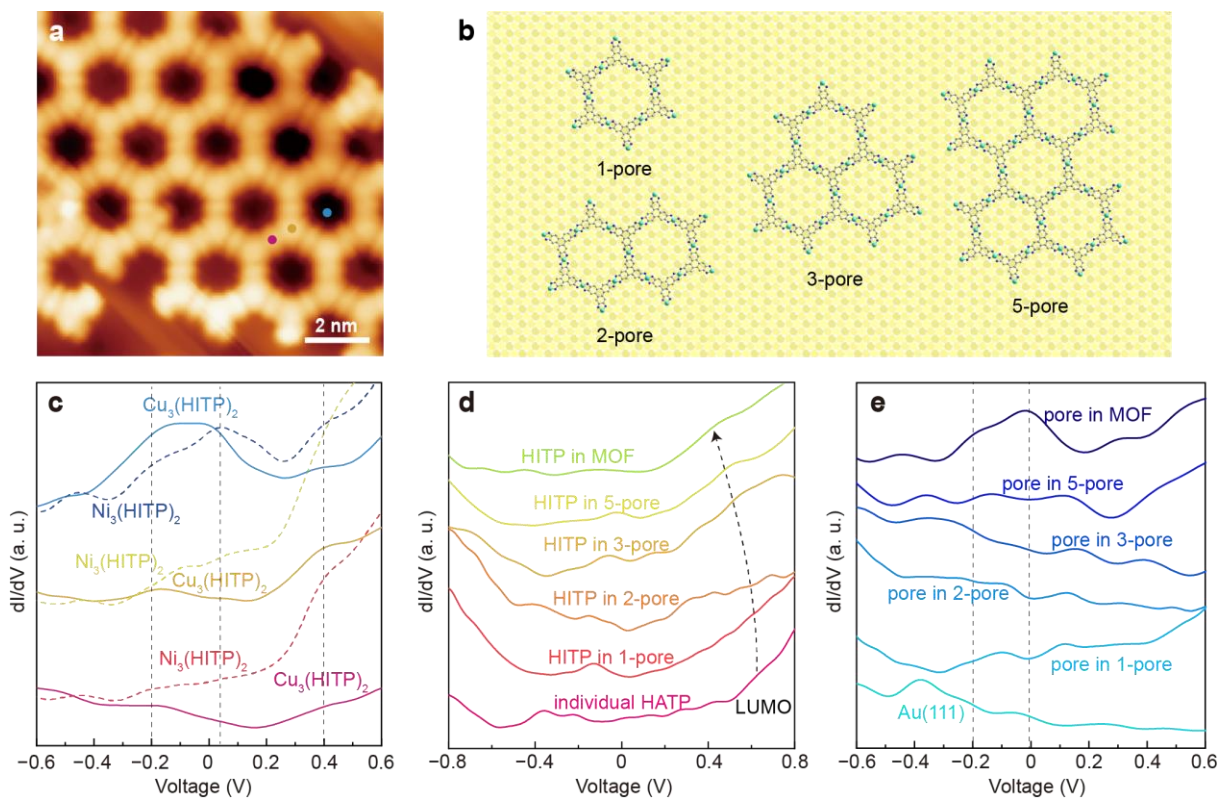


Fig. 5 | Size-dependent LDOS measurements of $M_3(\text{HITP})_2$ monolayers. **a**, STM topography of a $\text{Cu}_3(\text{HITP})_2$ domain. **b**, Configurations of MOF domains consisting of 1, 2, 3 and 5 pores. **c**, Comparative dI/dV spectra acquired at pore, ligand, and metal sites (color-coded in **a**) for both $\text{Cu}_3(\text{HITP})_2$ (solid lines) and $\text{Ni}_3(\text{HITP})_2$ (dashed lines). **d**, Evolution of dI/dV spectra at ligand sites of $\text{Ni}_3(\text{HITP})_2$: from an individual HATP molecule to ligands embedded in MOF domains consisting of 1, 2, 3, 5, and more than 10 pores. Discussions of DOS at different HITP sites are neglected due to their similar features. **e**, Evolution of dI/dV spectra at pore centers of $\text{Ni}_3(\text{HITP})_2$: from bare Au(111) substrate to pores in MOF domains consisting of 1, 2, 3, 5, and more than 10 pores. All the STM images and STS measurements were taken with $V_s = -1$ V, $I_t = 100$ pA.

Fermi level pinning

The lack of effective π - d conjugation at the Fermi level and the inefficient in-plane charge transport in monolayer $M_3(\text{HITP})_2$ seem to be contrary to common beliefs. Indeed, previous DFT band structure calculations of $\text{Ni}_3(\text{HITP})_2$ revealed a set of kagome bands right above the Fermi level and a flat band above 1 eV^{36,37}. The former is mainly derived from Ni orbitals with minor contribution from the ligand, whereas the latter is exclusively constructed by HITP

orbitals. Comparison between our results with the DFT band structure indicates that the large difference of work functions between the adsorbed $\text{Ni}_3(\text{HITP})_2$ and metal substrate likely causes abundant electron fillings from substrate towards the MOF and raises the Fermi level approximately 1 eV up to the energy gap between these bands. Such substrate-induced pinning effect results in the HITP-based flat band at 0.4 eV and the absence of Ni/Cu orbitals between -0.2 eV and 0.6 eV within the range of energies discussed in the above model (Supplementary Fig. 8). Therefore, band renormalization occurs in both components of the $\text{M}_3(\text{HITP})_2/\text{Au}(111)$ heterostructure.

To confirm the occurrence of Fermi level pinning, we compared dI/dV measurements of monolayer, large-area $\text{Ni}_3(\text{HITP})_2$ and $\text{Cu}_3(\text{HITP})_2$ on Au(111) containing at least 20 pores to explore the LDOS difference between these two MOFs at the metal nodes, center of HITP ligands, and center of pores, i.e. atomic sites that construct the above three types of lattices (Fig. 5a). LDOS at metal nodes and HITP ligands of these two MOFs are comparable: dI/dV spectra of both materials exhibit a prominent DOS peak at 0.4 eV and are featureless below -0.2 eV (Fig. 5c). At the center of pores, $\text{Ni}_3(\text{HITP})_2$ displays two broad DOS peaks at 0 eV and -0.2 eV that are absent at Ni and HITP sites. In $\text{Cu}_3(\text{HITP})_2$, the peak at -0.2 eV becomes more intense and merges with that at 0 eV. Previous DFT calculations on free-standing monolayer $\text{Ni}_3(\text{HITP})_2$ and $\text{Cu}_3(\text{HITP})_2$ predict semiconducting nature in the former and metallic behavior in the latter due to the band crossing at the Fermi level contributed by d electrons of Cu atoms³⁷. Nonetheless, our observation of comparable LDOS features of these two MOFs indicates that their Fermi levels are pinned by the gold substrate—the additional electrons from Cu mainly fill into electronic DOS within pores without significantly altering the band structure. The dominant contribution of gold to the Fermi level indicates that the electronic properties of MOF/metal heterostructures are determined by the metal substrate, whereas the MOF mainly provides the periodic and microporous architecture that modulates the surface states of substrate. Accordingly, the electron behaviors of MOF/metal interface can be altered rationally by selecting an appropriate substrate such that that specific band features of the MOF can be pinned to the Fermi level to improve electronic device performance.

Size-dependent electron behaviors

Crystallite size is known to strongly influence electrical properties of MOFs^{47,48}. To investigate the evolution of LUMO of HITP ligands with crystallite size, we compared the dI/dV spectra atop an individual HATP molecule, HITP ligands in small Ni₃(HITP)₂ crystallites containing 1, 2, 3, 5 hexagonal pores and extended MOF domains with more than 10 pores (Fig. 5b and Supplementary Fig. 1d–j). The DOS peak of HATP is located at 0.6 eV, corresponding to the LUMO of HATP on Au(111). As the size of crystallite increases, it gradually decreases to 0.4 eV atop HITP ligands at both center and edge of the crystallite (Fig. 5d and Supplementary Fig. 1d–j), indicating that extending the in-plane π -conjugation induces higher degrees of orbital hybridization and larger-scale electron hopping. Band renormalization shifts the respective orbital energies of ligands and metal ions towards each other, causing lower LUMO energy of HITP ligands in the heterostructure.

We further collected dI/dV spectra at center of pores in Ni₃(HITP)₂ crystallites with various sizes. No pronounced peak was observed near -0.2 eV or the Fermi level for the small crystallites, which is in sharp contrast to the spectrum acquired for larger crystallites (Fig. 5e). Hence, electron behaviors in smaller crystallites with less than 10 pores are vulnerable to the surrounding environments, preventing the emergence of resonant states in the pores—long-range modulated Au(111) surface electrons cannot be trapped densely inside nanostructures with insufficient lattice size and irregular surrounding scattering centers. Consequently, the complete triple-lattice electron hopping system cannot form within few-pore crystallites. In contrast, the resonant states are more robust in larger crystallites and could sustain even with irregular edges (Fig. 3a). Therefore, the formation of fully dispersive electronic bands and quantum corral networks in nanoscale M₃(HITP)₂ demands relatively large crystalline domains containing at least 10 pores. As nanoparticles of 2D conjugated MOFs are involved in many electronic devices^{7,9,15,32}, it is critical to control their sizes to optimize device performance.

Discussion

The forgoing results demonstrate band renormalization in both M₃(HITP)₂ and Au(111) surface upon the formation of epitaxial heterostructures. On one hand, the interfacial interaction

pins the Fermi level of $M_3(\text{HITP})_2$ and renormalizes its band structure, rendering the electronic states at the Fermi level dominated by the surface states of Au(111). On the other hand, interlayer electron-phonon coupling and lattice matching effectively modulate surface states of Au(111), generating flat bands and commensurate modulation that might lead to emergent phenomena such as strong correlation and charge density waves. The formation of a resonant state at the Fermi level coincidentally enhances the LDOS, inducing accumulation of charges derived from the substrate inside pores. Harnessing these effects could facilitate optimization of the MOF/electrode interface in electronic devices by tweaking structures and electronic properties of both constituents, potentially enhancing electrocatalytic activities and chemiresistive sensitivity among others. In addition, the pore-confined two-level resonant states might behave as qubits, and the quantum corral networks constructed by these states may be harnessed to simulate periodic systems. With structural regularity and tunability, MOF/metal heterostructures provide a great platform to investigate design principles of MOF-based electronic devices and to explore emergent physics and quantum simulation.

Materials and Methods

Sample preparation

HATP powder was synthesized based on literature procedures¹³. An atomically clean Au(111) surface was prepared by repeated argon ion sputtering and annealing at 540 °C. For $\text{Ni}_3(\text{HITP})_2$ growth, Ni was firstly deposited onto Au substrate held at room temperature for 30 s under a background pressure of 10^{-9} mbar, resulting in a sub-monolayer Ni coverage exceeding 20%. HATP organic ligands were then evaporated at 160 °C from crucibles for 20 s onto the substrate held at room temperature in a separate chamber at 10^{-6} mbar. The sample was subsequently annealed at 240 °C for 15 minutes under ultra-high vacuum (10^{-10} mbar) to form the self-assembly of large-area monolayer $\text{Ni}_3(\text{HITP})_2$ films. $\text{Cu}_3(\text{HITP})_2$ was synthesized under similar conditions by substituting Ni with Cu at lower sublimation temperature. The lateral size of the MOF single crystals was controlled by varying the HATP deposition time. Shorter exposures yielded smaller domains with few pores. The formation of MOFs is independent on the deposition sequence of metal atoms and molecular ligands.

STM measurements

All the STM and spectroscopic measurements were performed using a commercial low-temperature STM (Infinity STM, Omicron) at 12.5 K under a base pressure of approximately 7.0×10^{-11} mbar. Topographic images, STS line spectra, and mappings were acquired in constant-current mode with $V = -1$ V and $I = 100$ pA setpoint. The dI/dV spectra were measured by using lock-in technology with an AC voltage of 25 mV and a superimposed frequency of 790 Hz on the bias voltage. The STM tip condition was verified by the surface state appearance of clean Au(111). QPI patterns were taken by FFT analysis of STS mappings in momentum space at varied energies.

q-Plus AFM measurements

q-Plus AFM measurements were performed with an Omicron Infinity low-temperature STM at 12.5 K under a base pressure 10^{-11} mbar. A CO-functionalized tip was prepared by picking up an adsorbed CO molecule from Au(111) substrate when scanning with setpoint at $V = 100$ mV and $I = 100$ pA. Successful tip functionalization was confirmed by imaging individual CO molecules with altered topography.

Data processing

All STM and AFM images were processed using WSxM software⁴⁹. Spectra were appropriately smoothed to remove background thermal noise.

Data availability

The data that support the findings of this study are available from the corresponding author upon request.

References

1. Fu, S. *et al.* Fundamentals of charge transport in two-dimensional framework materials. *Nat. Rev. Mater.* (2025), doi: 10.1038/s41578-025-00840-z.
2. Huang, X. *et al.* Superconductivity in a Copper(II)-Based Coordination Polymer with Perfect Kagome Structure. *Angew. Chem. Int. Ed.* **57**, 146–150 (2018).

3. Dou, J.-H. *et al.* Signature of Metallic Behavior in the Metal–Organic Frameworks $M_3(\text{hexaiminobenzene})_2$ ($M = \text{Ni}, \text{Cu}$). *J. Am. Chem. Soc.* **139**, 13608–13611 (2017).
4. Sporrer, L. *et al.* Near IR Bandgap Semiconducting 2D Conjugated Metal - Organic Framework with Rhombic Lattice and High Mobility. *Angew. Chem. Int. Ed.* **62**, e202300186 (2023).
5. Wang, Z., Wang, M., Heine, T. & Feng, X. Electronic and quantum properties of organic two-dimensional crystals. *Nat. Rev. Mater.* **10**, 147–166 (2025).
6. Pan, Z. *et al.* Synthesis and structure of a non-van-der-Waals two-dimensional coordination polymer with superconductivity. *Nat. Commun.* **15**, 9342 (2024).
7. Dong, R. *et al.* High-mobility band-like charge transport in a semiconducting two-dimensional metal–organic framework. *Nat. Mater.* **17**, 1027–1032 (2018).
8. Wang, Z. F., Liu, Z. & Liu, F. Organic topological insulators in organometallic lattices. *Nat. Commun.* **4**, 1471 (2013).
9. Campbell, M. G., Sheberla, D., Liu, S. F., Swager, T. M. & Dincă, M. $\text{Cu}_3(\text{hexaiminotriphenylene})_2$: An Electrically Conductive 2D Metal–Organic Framework for Chemiresistive Sensing. *Angew. Chem. Int. Ed.* **127**, 4423–4426 (2015).
10. Niu, L. *et al.* Conductive Metal–Organic Frameworks for Supercapacitors. *Adv. Mater.* **34**, e2200999 (2022).
11. Cheng, W.-Z. *et al.* Bifunctional iron-phtalocyanine metal–organic framework catalyst for ORR, OER and rechargeable zinc–air battery. *Rare Met.* **39**, 815–823 (2020).
12. Clough, A. J., Yoo, J. W., Mecklenburg, M. H. & Marinescu, S. C. Two-Dimensional Metal–Organic Surfaces for Efficient Hydrogen Evolution from Water. *J. Am. Chem. Soc.* **137**, 118–121 (2015).
13. Smith, M. K. & Mirica, K. A. Self-Organized Frameworks on Textiles (SOFT): Conductive Fabrics for Simultaneous Sensing, Capture, and Filtration of Gases. *J. Am. Chem. Soc.* **139**, 16759–16767 (2017).

14. Koo, W.-T., Jang, J.-S. & Kim, I.-D. Metal–Organic Frameworks for Chemiresistive Sensors. *Chem* **5**, 1938–1963 (2019).
15. Sheberla, D. *et al.* Conductive MOF electrodes for stable supercapacitors with high areal capacitance. *Nat. Mater.* **16**, 220–224 (2017).
16. Wu, G., Huang, J., Zang, Y., He, J. & Xu, G. Porous Field-Effect Transistors Based on a Semiconductive Metal–Organic Framework. *J. Am. Chem. Soc.* **139**, 1360–1363 (2017).
17. Liu, Y. *et al.* Approaching the Schottky–Mott limit in van der Waals metal–semiconductor junctions. *Nature* **557**, 696–700 (2018).
18. Zhao, W.-M. *et al.* Moiré enhanced charge density wave state in twisted 1T-TiTe₂/1T-TiSe₂ heterostructures. *Nat. Mater.* **21**, 284–289 (2022).
19. Jia, C. *et al.* Ferroelectrically Modulated and Enhanced Photoresponse in a Self-Powered α In₂Se₃/Si Heterojunction Photodetector. *ACS Nano* **17**, 6534–6544 (2023).
20. Li, Y. *et al.* 1D Electronic Flat Bands in Untwisted Moiré Superlattices. *Adv. Mater.* **35**, e2300572 (2023).
21. McGilly, L. J. *et al.* Visualization of moiré superlattices. *Nat. Nanotechnol.* **15**, 580–584 (2020).
22. Lowe, B. *et al.* Local gate control of Mott metal-insulator transition in a 2D metal-organic framework. *Nat. Commun.* **15**, 3559 (2024).
23. Lian, Y. *et al.* Unpaired 3d Electrons on Atomically Dispersed Cobalt Centres in Coordination Polymers Regulate both Oxygen Reduction Reaction (ORR) Activity and Selectivity for Use in Zinc–Air Batteries. *Angew. Chem. Int. Ed.* **59**, 286–294 (2020).
24. Zhao, B., Zhang, J., Feng, W., Yao, Y. & Yang, Z. Quantum spin Hall and Z₂ metallic states in an organic material. *Phys. Rev. B* **90**, 201403 (2014).
25. Sheberla, D. *et al.* High Electrical Conductivity in Ni₃(2,3,6,7,10,11-hexaiminotriphenylene)₂, a Semiconducting Metal–Organic Graphene Analogue. *J. Am. Chem. Soc.* **136**, 8859–8862 (2014).

26. Wu, M. *et al.* Conetronics in 2D metal-organic frameworks: double/half Dirac cones and quantum anomalous Hall effect. *2D Mater.* **4**, 015015 (2016).
27. Wang, Z. F., Su, N. & Liu, F. Prediction of a Two-Dimensional Organic Topological Insulator. *Nano Lett.* **13**, 2842–2845 (2013).
28. Zhang, L. Z. *et al.* Intrinsic Two-Dimensional Organic Topological Insulators in Metal–Dicyanoanthracene Lattices. *Nano Lett.* **16**, 2072–2075 (2016).
29. Jing, Y. & Heine, T. Two-Dimensional Kagome Lattices Made of Hetero Triangulenes Are Dirac Semimetals or Single-Band Semiconductors. *J. Am. Chem. Soc.* **141**, 743–747 (2019).
30. Chen, T. *et al.* Continuous Electrical Conductivity Variation in $M_3(\text{Hexaiminotriphenylene})_2$ ($M = \text{Co, Ni, Cu}$) MOF Alloys. *J. Am. Chem. Soc.* **142**, 12367–12373 (2020).
31. Nakaza, S., Shi, Y., Zhang, Z., Akbar, S. & Shakib, F. A. Two-Dimensional Electrically Conductive Metal–Organic Frameworks: Insights and Guidelines from Theory. *Acc. Chem. Res.* **58**, 3021–3032 (2025).
32. Miner, E. M. *et al.* Electrochemical oxygen reduction catalysed by $\text{Ni}_3(\text{hexaiminotriphenylene})_2$. *Nat. Commun.* **7**, 10942 (2016).
33. Gu, F., Shu, S., Patrick, C. E. & Castell, M. R. Scanning Tunneling Microscopy of Bimetallic Ni/Co-HITP Metal–Organic Framework Monolayers. *J. Phys. Chem. C* **128**, 17797–17805 (2024).
34. Lischka, M. *et al.* Competitive Metal Coordination of Hexaaminotriphenylene on Cu(111) by Intrinsic Copper Versus Extrinsic Nickel Adatoms. *Chem. A Eur. J.* **25**, 1975–1983 (2019).
35. Gao, Z. *et al.* Synthesis and characterization of a single-layer conjugated metal–organic structure featuring a non-trivial topological gap. *Nanoscale* **11**, 878–881 (2018).
36. Chen, J. *et al.* Two-Dimensional Conjugated Metal–Organic Framework/Graphene π – π Stacked Heterostructures for Ultrafast Photonics. *Adv. Funct. Mater.* **34**, 2313027 (2024).

37. Chen, S., Dai, J. & Zeng, X. C. Metal–organic Kagome lattices $M_3(2,3,6,7,10,11\text{-hexaminotriphenylene})_2$ ($M = \text{Ni}$ and Cu): from semiconducting to metallic by metal substitution. *Phys. Chem. Chem. Phys.* **17**, 5954–5958 (2015).
38. Gao, Z. *et al.* Design and Synthesis of a Single-Layer Ferromagnetic Metal–Organic Framework with Topological Nontrivial Gaps. *J. Phys. Chem. C* **124**, 27017–27023 (2020).
39. Reinert, F., Nicolay, G., Schmidt, S., Ehm, D. & Hüfner, S. Direct measurements of the L-gap surface states on the (111) face of noble metals by photoelectron spectroscopy. *Phys. Rev. B* **63**, 115415 (2001).
40. Schouteden, K., Lievens, P. & Haesendonck, C. V. Fourier-transform scanning tunneling microscopy investigation of the energy versus wave vector dispersion of electrons at the Au(111) surface. *Phys. Rev. B* **79**, 195409 (2009).
41. Zhang, Y. *et al.* Enhancement of the performance of Ge–air batteries under high temperatures using conductive MOF-modified Ge anodes. *Carbon Energy* **6**, e580 (2024).
42. Akram, W. *et al.* Metal Organic Framework based Humidity Sensing: Stability, performance, and IoT Integration. *J. Sci.: Adv. Mater. Devices* **10**, 100972 (2025).
43. Crommie, M. F., Lutz, C. P. & Eigler, D. M. Confinement of Electrons to Quantum Corrals on a Metal Surface. *Science* **262**, 218–220 (1993).
44. Chen, H. *et al.* Visualizing Interfacial Charge Trapping in a Heterostructure of a Monolayer Metal–Organic Framework on a van der Waals Substrate. *J. Am. Chem. Soc.* **148**, 6193–6199 (2026).
45. Piquero-Zulaica, I. *et al.* Engineering quantum states and electronic landscapes through surface molecular nanoarchitectures. *Rev. Mod. Phys.* **94**, 045008 (2022).
46. Klappenberger, F. *et al.* Tunable Quantum Dot Arrays Formed from Self-Assembled Metal–Organic Networks. *Phys. Rev. Lett.* **106**, 026802 (2011).
47. Khaliq, F. *et al.* Size-Dependent Optical Band Gaps in Metal–Organic Framework Nanoparticles. *J. Am. Chem. Soc.* **147**, 45748–45762 (2025).

48. Grape, E. S., Davenport, A. M., Kadota, K., Horike, S. & Brozek, C. K. Crystallographic Evidence of Size-Dependent Bond Flexibility in Metal–Organic Framework Nanocrystals. *ACS Materials Lett.* **7**, 3893–3900 (2025).

49. Horcas, I. *et al.* WSXM: A software for scanning probe microscopy and a tool for nanotechnology. *Rev. Sci. Instrum.* **78**, 013705 (2007).

Acknowledgments

This work was financially supported by the Zhejiang Provincial Natural Science Foundation of China (XHD23B0301). We thank Huiru Liu for assistance with STM experiments, Prof. Wei Zhu for theoretical suggestions, Dr. Jiaqi Lin for helpful discussions on QPI analysis, and Prof. Yi Du for experimental instructions. L.S. thanks Prof. Zhongyue Zhang, Prof. Jin-Hu Dou, Prof. Xiaohui Qiu, Prof. Mengxi Liu, Prof. Carl K. Brozek, Prof. Jie Wu, and Prof. Shuigang Xu for helpful discussions.

Author contributions

S. W. and L. S. conceived the idea and designed the experiments. X. Y., S. W., and X. H. conducted the MBE growth of $M_3(\text{HITP})_2$ and subsequent STM & q-Plus AFM characterization. Z. S. synthesized the HATP molecules. All the experiments were done at Songshan Lake Materials Laboratory. S. W. performed the theoretical calculations. S. W., X. Y., and L. S. analyzed the experimental data and wrote the manuscript. All the authors contributed to the data analysis and provided feedback on the manuscript.

Competing interests

The authors declare no competing interests.

Additional information

Supplementary information